# Topographic Rossby Wave-modulated oscillations of dense overflows

Xianxian Han[1,2], Andrew L. Stewart[3], Dake Chen*[2,4,5], Tao Lian[2,4,5], Xiaohui Liu[2,4], Xiaohui Xie[2,4,5]

1 State Key Laboratory of Marine Environmental Science, College of Ocean and Earth Sciences, Xiamen University, Xiamen, China
2 State Key Laboratory of Satellite Ocean Environment Dynamics, Second Institute of Oceanography, Ministry of Natural Resources, China
3 Department of Atmospheric and Oceanic Sciences, University of California, Los Angeles, California, USA
4 Southern Marine Science and Engineering Guangdong Laboratory (Zhuhai), China
5 School of Oceanography, Shanghai Jiaotong University, Shanghai, China

Corresponding to: dchen@sio.org.cn

## Key points

Baroclinic instability of dense overflows energizes coupled Topographic Rossby Waves (TRWs), which oscillate throughout the water column.

For small topographic slopes, TRWs can feed back to the outflow and instigate the formation of coherent, dense eddies.

Steep slopes can suppress the formation of TRWs and eddies, decreasing the amplitude of dense overflow variability.

## Abstract

The global supply of Antarctic Bottom Water (AABW) is sourced from a handful of dense overflows. Observations from the Weddell Sea indicate that the overflow there exhibits prominent oscillations accompanied by dense eddies, while the Ross Sea overflow shows no significant oscillations other than tides, yet the genesis of these oscillations and their role in mediating AABW export remain poorly understood. Here idealized model simulations are used to investigate the

dynamics of these oscillations. It is shown that the dominant oscillations result from the formation of Topographic Rossby Waves (TRWs) associated with baroclinic instability of the dense overflow. A key finding is that the TRWs can feed back onto the dense overflow, producing coherent subsurface eddies of the same frequency. A series of sensitivity experiments reveal that these behaviors depend strongly on the local environment: steep topographic slopes suppress the baroclinic growth of TRWs, while strong downstream along-slope flows suppress the upstream propagation of TRW energy and genesis of subsurface eddies. These results explain the varying prevalence of different oscillatory phenomena observed across different dense overflow regimes.

## Plain Language Summary

Antarctic Bottom Water (AABW) comprises the densest water in the major ocean basins, filling more than one-third of the ocean. AABW is sourced from dense water spilling into the deep ocean at several specific sites around the Antarctic coast, referred to as “overflows”. These overflows have been observed to coincide with energetic fluctuations of water across the Antarctic continental slope, which separates the relatively shallow waters around the Antarctic continent from the deep waters of the open ocean. However, the mechanism via which these fluctuations are generated, and their interaction with the overflows of dense waters, remain poorly understood. This study identifies a range of behaviors over the continental slope, ranging from no fluctuations at all, to wave-like fluctuations across the continental slope, to the formation of horizontal vortices. The transitions between these behaviors are shown to depend on the local environmental conditions, notably the steepness of the continental slope and the speed of the ambient flow along the continental slope. These findings are in good agreement with in-situ observations and help to explain the range of behaviors observed in overflows in nature.

## 1. Introduction

Antarctic Bottom Water (AABW) is the coldest, densest major water mass, filling 30-40% of

the subsurface ocean (Johnson, 2008). It originates from the dense shelf water (DSW) formed in several specific regions along the Antarctic coast – primarily in the Weddell Sea (Foldvik et al., 2004), the Ross Sea (Gordon et al., 2009), the Adelie coast (Williams et al., 2008), and Prydz Bay (Ohshima et al., 2013) – via brine rejection from sea ice growth and mixing with ice shelf meltwater. Due to its relatively high density, DSW overflows across the shelf break, descends down the continental slope and mixes with ambient waters to produce AABW (Legg et al., 2009). This process drives the lower cell of the meridional overturning circulation (Talley, 2013), and thus plays a key role in the maintenance and variability of the global ocean circulation and climate.

In situ observations show that the dense overflow in the southern Weddell Sea exhibits energetic oscillations, comprised of cold, bottom-trapped eddies (Jensen et al., 2013; Daae et al., 2019). The oscillations consist of strong tidal signals and three other subinertial frequencies with periods of ~35 hours, ~3 days and ~6 days respectively. These subinertial oscillations are associated with nearly barotropic vertical structures, and there is a tendency for shorter-period oscillations to be more energetic over the upper continental slope (Darelius et al., 2009). As shown in Fig. 1(a-b), among four sets of moorings (Fahrbach et al., 1998a-d; Fer, 2016a-e; Foldvik, 2017a-b; Woodgate et al., 2017a-b), those located over the upper slope exhibit non-tidal oscillations with a dominant period of ~35 hours in the near-bottom flows. Similar phenomena have been observed in other overflow regions, such as the Prydz Bay (Oshima et al., 2013), the Denmark Strait (Spall and Price, 1998) and the Faroe Bank Channel (Darelius et al., 2015). In contrast, the Ross Sea overflow shows no significant subtidal oscillations except for mooring EB, which shows a weak signal around a period of 35 hours, as shown in Fig. 1(c-d). Oscillations of dense overflows can potentially affect the descent rate and properties of AABW.

A number of possible explanations for the subtidal oscillations have been suggested, including baroclinic instability (Swaters, 1991; Reszka et al., 2002; Guo et al., 2014), vortex stretching (Spall and Price, 1998; Marques et al., 2014) and generation of Topographic Rossby Waves (TRWs) (Jensen et al., 2013; Marques et al., 2014; Nakayama et al., 2014). These mechanisms are not

mutually exclusive: all of them could be at work in overflows across the continental slope, e.g. the baroclinic instability takes the form of growing TRWs in the overlying water (Swaters, 1991). However, it remains unclear how the manifestation of these processes is controlled by environmental conditions, and how the resulting oscillations feed back on the export of DSW.

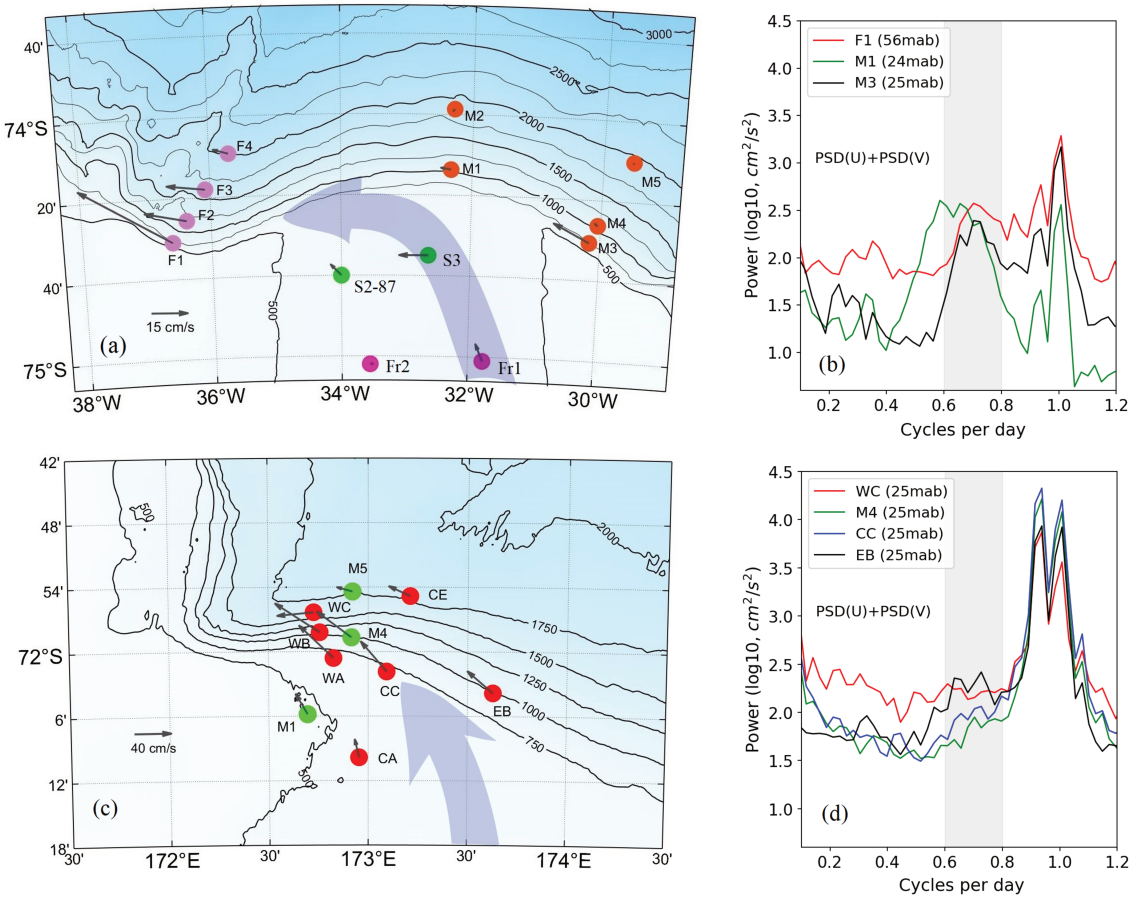


Figure 1. (**a**) Historical mooring sites in Weddell Sea overflow: the F1-4 moorings deployed in 1998; the M1-5 moorings deployed in 2009; the S2-87 mooring deployed in 1987; the S3 mooring deployed in 1992; and the Fr1-2 moorings deployed in 1995. The black arrows indicate time averaged flow measured by the near-bottom instruments (all within 70 meters above bottom (mab)); (**b**) Power spectra of the velocity from the moorings over the upper continental slope. Grey shading indicates periods between 30 and 40 hours; (**c**) Historical mooring sites in Ross Sea overflow: the red dots indicate moorings deployed in 2003; the green dots indicate moorings deployed in 2004. Arrows indicate the mean flow during neap tide (3 days); (**d**) Power spectra of the velocity from the moorings on the continental slope.

In this paper, we use idealized numerical simulations to investigate oscillatory phenomena

(excluding tides) occurring in different DSW export regimes. In Section 2, we formulate an idealized model to allow exploration of a wide range overflow dynamical regimes. In Section 3, we show that in a configuration representative of the southern Weddell Sea, the oscillations take the form of coupled TRWs associated with baroclinic instability of dense overflow. These TRWs lead to the formation of subsurface dense eddies in a Weddell-like, but not a Ross-like, parameter regime. We further quantify the transitions between steady, wavy and eddying regimes across a range of along-slope flow speeds and slope steepnesses. Finally, in Section 4 we discuss our findings and provide concluding remarks.

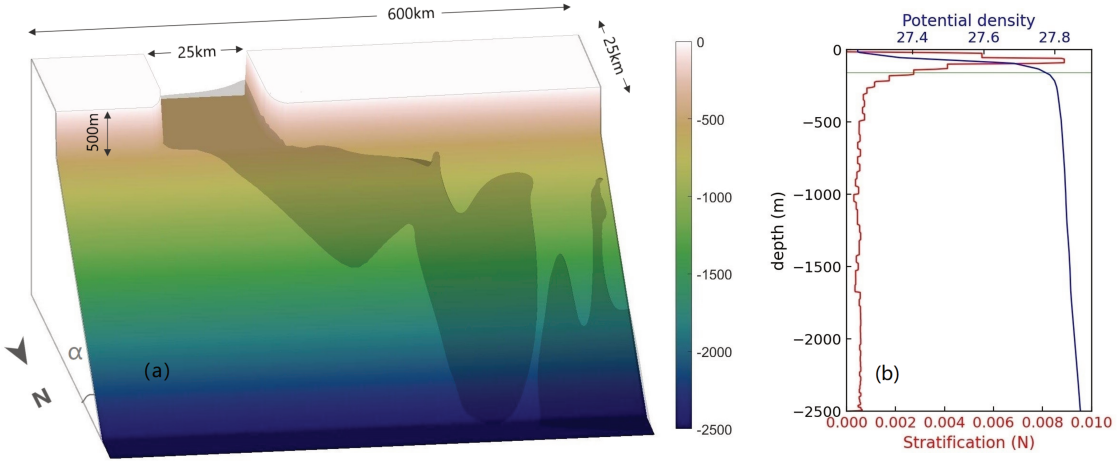


Figure 2. (**a**) Schematic showing the model bathymetry and overflow, with continental slope steepness $s = tan\,\alpha$. The grey shading indicates an instantaneous snapshot of a 3D density surface, representing the upper boundary of the dense shelf water overflow; (**b**) Initial potential density and buoyancy frequency profiles. The green line indicates the nominal pycnocline depth.

## 2. Model configuration

The model we use is the Regional Ocean Modeling System (ROMS), selected for its fidelity in representing oceanic flows over steep slopes (Shchepetkin and McWilliams, 2003; Ilicak et al., 2012). For clarity and generality, we use a model domain with idealized bathymetry, as shown in Fig. 2(a). In our reference simulation, the model domain (600 x 250 km) consists of a 500m-deep trough at the southern boundary, connected via a linear slope (with slope angle $s = 1/15$) to a flat

abyssal ocean of 2500m depth. This slope angle has been selected to approximate the upper continental slope in the Weddell Sea. The model is eddy resolving, having a horizontal resolution of 0.5km (Stewart and Thompson, 2015) near the trough region, stretching to 2km near the offshore boundary. The vertical discretization uses 60 topography-following levels with increased resolution close to the sea floor (~5m over the upper slope, where the typical overflow thickness is over 100m). The initial stratification is adapted from in situ observations in the Ross Sea (Station 47, Gordon et al., 2009), with relatively strong stratification in the upper 150m and a weaker, approximately constant stratification ($\mathrm{N} \sim 6 \times 10^{-4}\ s^{-2}$) below (Fig. 2(b)). A constant Coriolis parameter of $f = -1.38 \times 10^{-4}$ (72°S) is used throughout the model domain.

An inflow of DSW with uniform potential temperature (-1.8°C) and salinity (34.8 psu) (Gordon et al., 2009) is prescribed at the southern end of the trough. To ensure that the structure of the inflow changes as little as possible within the trough, we follow the geostrophic inflow prescription of Legg et al. (2006). The inflow then has its maximum thickness (150 m) and velocity (~0.4 m/s) at the left-hand wall (looking northward), and the thickness decays exponentially with a length scale of deformation radius (~5 km, Fig. 2(a)). The dense inflow flux is around 0.2Sv, which is relatively small compared to the observed Ross Sea overflow (~0.8Sv, Gordon et al., 2009) and Weddell Sea overflow (1.6±0.5Sv, Foldvik et al., 2004), but not unreasonable considering that this is a highly idealized model of dense water formation. To track the DSW plume, we inject a passive tracer with initial concentration of 1 kg/m$^3$ with the dense inflowing water. In the reference simulation there is no other forcing: the eastern, western and northern boundaries all use radiation conditions. We also run simulations to investigate the impact of an imposed along-slope flow, representing the presence of the Antarctic Slope Current, with a barotropic flow prescribed at both eastern and western boundaries. All simulations are integrated until steady state is reached, as indicated by steady oscillations in the model state variables, which typically occurs after ~30 days. We then analyze the last ~10 days of integration using hourly-averaged model output.

## 3. Results

The phenomenology of the overflow in our reference simulation is illustrated in Fig. 3(a-c). The dense inflow moves northward through the trough, then begins to flow downslope while turning left under the influence of the Coriolis force. Over the slope the overflow interacts with the overlying waters, producing wave-like westward-propagating oscillations throughout the water column. Associated with the negative phase of these oscillations are strong patches of negative vorticity, corresponding to areas of higher depth-integrated tracer concentration near the coast, suggesting the existence of dense eddies. All of these are consistent with in-situ observations in the Weddell Sea (Darelius et al., 2009; Jensen et al., 2013; Daae et al., 2019). When a westward background flow of 6 cm/s is prescribed (Fig. 3(d-f)), the oscillations become much weaker and the dense eddies disappear. When the slope steepness is doubled (Fig. 3(g-i)), the oscillations are no longer evident and the overflow forms an approximately steady westward current confined to the slope, which is consistent with in-situ observations in the Ross Sea overflow (Fig. 1(c-d)). The strong influence of background flow and topography on the overflow oscillations can also be clearly seen in Fig. 3(j). In the following subsections we separately analyze the simulated TRWs and cyclonic eddies, and characterize the overflow oscillations across a range of slope steepnesses and background flows.

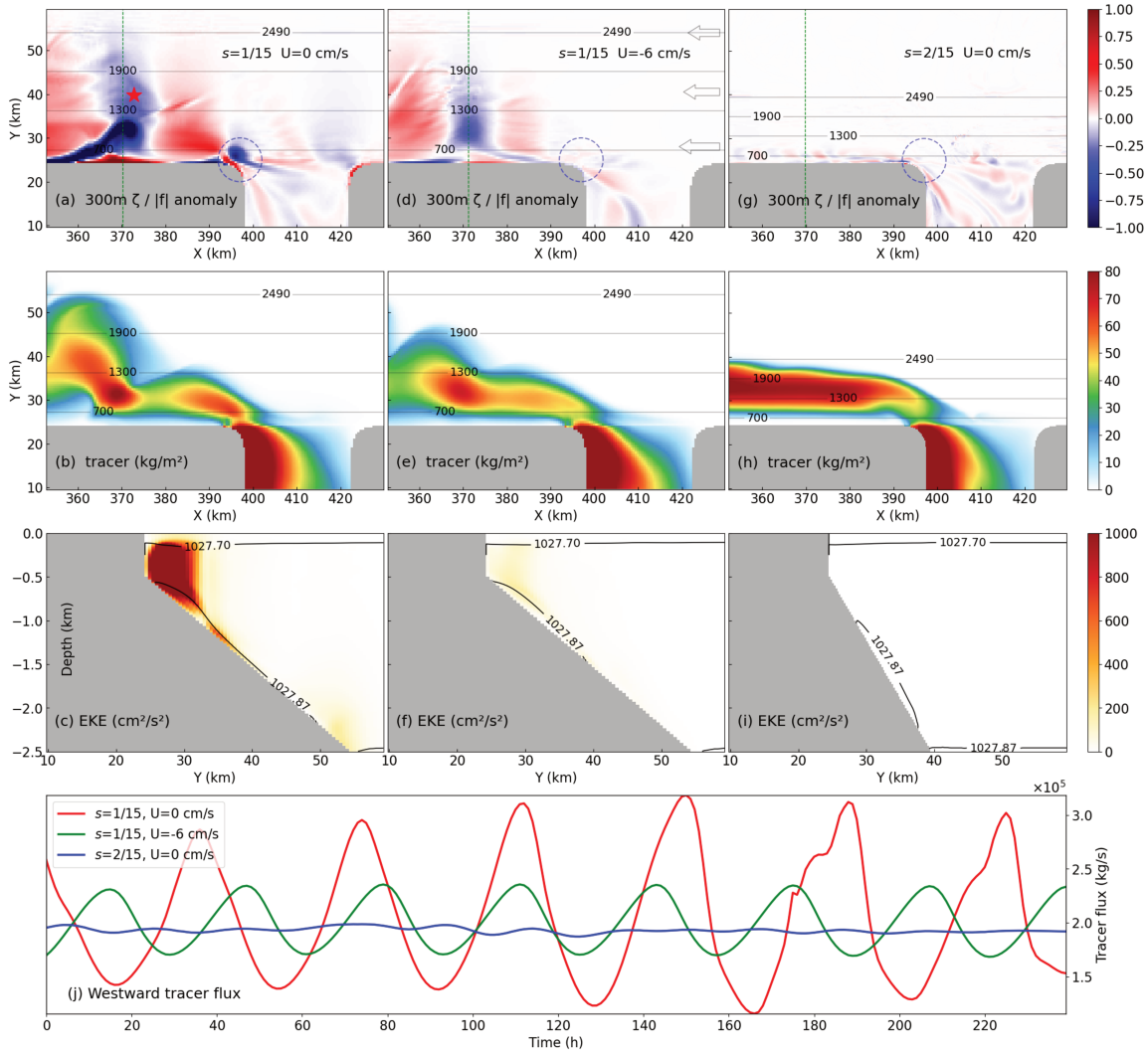


Figure 3. Diagnostics from three simulations, illustrating the effects of background along-slope flow and varying slope steepness. **(a)** Snapshot of normalized vertical relative vorticity ($\zeta/|f|$) anomaly (relative to a 6-cycle time average) at 300m depth. Gray contours indicate the bathymetry. The green line indicates the location of the vertical profile shown in panel (c), and the red star indicates the location used to diagnose the simulated TRW properties. The dashed blue circle indicates the generation site of the subsurface eddies; **(b)** Depth-integrated tracer concentration corresponding to panel (a); **(c)** Cross-slope/vertical distribution of eddy kinetic energy across the section indicated by the green line in panel (a). Contours show surface-referenced potential density; **(d-f)** As panels (a-c), but for a simulation with a westward background flow of 6 cm/s near the coast that decreases linearly to zero at the northern boundary (indicated by arrows at the eastern boundary in panel (d)); **(g-i)** As panels (a-c), but for a simulation with a steeper slope of $s = 2/15$; **(j)** Time series of westward tracer flux, integrated across the cross-slope/depth section 25km downstream from the trough (green dashed lines shown in panels a, d, and g).

### 3.1 Coupled TRWs associated with baroclinic instability

Previous studies based on numerical simulations (Marques et al., 2014; Nakayama et al., 2014) and observations (e.g. Jensen et al., 2013) have identified the oscillations associated with dense overflows as TRWs. Motivated by these studies, we first examine whether the simulated oscillations satisfy the linear TRW theory (Pedlosky, 1987; Zhao et al., 2018). For simplicity, we assume a constant stratification $N_0$ ($6 \times 10^{-4}\ s^{-2}$), and treat $z$ = -150 m as a rigid lid. Then the dispersion relationship for plane TRWs in the presence of a uniform background flow ($U$) (Pedlosky, 1987) can be expressed as

$$\omega = Uk + \frac{N_0 sk}{K\tanh\left(\frac{N_0 K}{f_0} H\right)} \qquad (1)$$

where $H$ is the water column thickness (below 150m depth) and $K = k$ (we assume meridional wavenumber $l = 0$). The group velocity of the waves is given by $c_g = \partial\omega/\partial k$.

To diagnose the properties of the simulated waves, we choose a location indicated by the red star in Fig. 3(a), which lies in the middle of the slope and 25km downstream of the trough, where the waves have reached a relatively mature state. We estimate the wave frequency by Fourier spectral analysis and compare it to that predicted by Equation (1), using $N_0 = 6 \times 10^{-4}\ s^{-2}$, $s = 1/15$, $k = -1.9 \times 10^{-4}\ m^{-1}$, $f = -1.38 \times 10^{-4}$, $H = 1350\ m$, $U = 0\ cm/s$. Here we obtain the zonal wavenumber $k$ directly from the model output, by computing the time-averaged distance between the nearest wave peak and trough of the meridional velocity. For these parameters, Equation (1) predicts an oscillation period of ~35h, which is close to that diagnosed from our simulation (~38h, Fig. 3(j), red curve) and to the observation (~35h) in the Weddell Sea. Based on this and our sensitivity experiments (see Section 3.3), we conclude that the waves approximately satisfy the TRW theory. Using the same parameters, the group velocity of TRWs is positive (13 cm/s), indicating eastward wave energy propagation (Jensen et al., 2013; Marques et al., 2014). This explains the presence of the wave signals upstream of the trough (Fig. 1(b) and Fig. 3(a)).

The TRWs ultimately source their energy from the DSW overflow, i.e. from the release of potential energy as the dense water descends the slope. Given that the resulting flows are approximately geostrophic, this suggests that baroclinic instability of the DSW may be responsible for generating the TRWs (Pedlosky 1987). We therefore interpret the genesis of the TRWs using theory of Swaters (1991), which describes the linear baroclinic instability of a dense fluid layer on a bathymetric slope, underlying a quasi-geostrophic ambient fluid of lighter density. This theory suggests that the instability takes the form of growing waves in the DSW layer that are coupled to growing TRWs in the overlying fluid. A necessary condition for baroclinic instability to occur is that the slope ratio ($\delta$) between isopycnal slope ($s_\rho$) and topographic slope ($s$) is larger than one, i.e. $\delta = \frac{s_\rho}{s} > 1$ (Swaters, 1991; Isachsen 2015). Figs. 4(a-b) show that this condition is satisfied in both our reference simulation and in the case with a topographic slope of $s = 2/15$. In contrast, the $s = 2/15$ simulation exhibits negligible oscillations in the along-slope DSW transport, with the dense overflows taking the form of steady along-slope flow instead (Fig. 3(g-j)), indicating that the instability has been suppressed.

To assesss whether the TRWs are indeed generated via baroclinic instabilities, we formulate a budget for the eddy kinetic energy (EKE) (Gula et al., 2016; Stewart and Thompson, 2016):

$$\frac{\partial}{\partial t}\mathrm{EKE} = \underbrace{-\nabla \cdot T_{eke}}_{convergence} + \underbrace{(\mathrm{MKE} \rightarrow \mathrm{EKE})}_{barotropic} + \underbrace{(\mathrm{PE} \rightarrow \mathrm{EKE})}_{baroclinic} + Dissipation\,, \quad (2)$$

$$\mathrm{EKE} = \frac{1}{2}\left(\overline{u'^2 + v'^2}\right), \quad (3)$$

$$T_{eke} = \frac{1}{2}\left(\overline{\boldsymbol{u}_h'^2 \cdot \boldsymbol{u}}\right) + \frac{1}{\rho_0}\left(\overline{\boldsymbol{u}' p'}\right), \quad (4)$$

$$\mathrm{MKE} \rightarrow \mathrm{EKE} = -\overline{\boldsymbol{u}_h' \cdot (\boldsymbol{u}' \cdot \nabla)\overline{\boldsymbol{u}_h}}, \quad (5)$$

$$\mathrm{PE} \rightarrow \mathrm{EKE} = \overline{w' b'}. \quad (6)$$

Here $\boldsymbol{u_h} = (u, v)$, $\boldsymbol{u} = (u, v, w)$, $b = -\frac{g\rho}{\rho_0}$, $p$ is pressure, the overbar indicates a time average over 6 wave periods, and the prime denotes perturbations from the mean. Note that, by this definition,

211 the EKE quantifies the energy associated with all deviations from the mean over several wave
212 periods, which includes both the nonlinear eddies (when they are present) and the TRWs. The
213 underbraces in equation (2) identify three energy tendency terms, due to energy flux convergence
214 (this will be used in section 3.2), barotropic conversion from the mean flow, and baroclinic
215 production, respectively. Diagnostics of these terms from our simulations show that the baroclinic
216 and barotropic energy conversions are both negligibly small for steep slope case (Fig. 4(b-c)),
217 consistent with the approximate absence of TRWs. In the reference case EKE is produced over the
218 continental slope via both baroclinic and barotropic conversions (Fig. 4(e-f)), but baroclinic
219 conversion dominates (volume integrals yield $-2.2 \times 10^7\, J/s$ and $9.2 \times 10^7\, J/s$ for barotropic and
220 baroclinic conversions respectively). These diagnostics support our characterization of the waves in
221 our simulations are coupled TRWs associated with baroclinic instability of the dense overflow. In
222 Sec. 3.3 we posit an alternative explanation for the suppression of TRWs for steep bathymetric
223 slopes based on our sensitivity experiments.
224

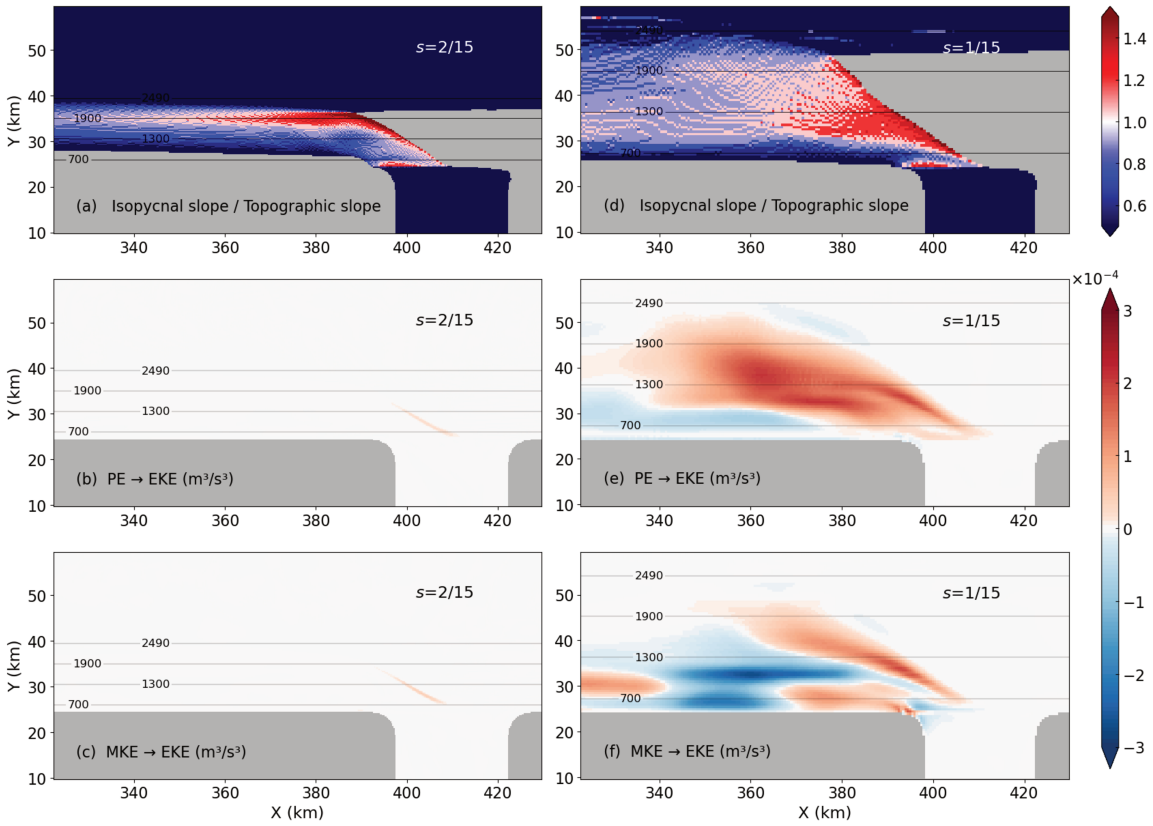


225

226 Figure 4. Topographic effect on energy conversion. Left side panels correspond to an experiment with slope
227 angle of $s = 2/15$, and right-side panels correspond to our reference experiment. Contours indicate
228 bathymetric depths in meters. (**a,d**) Slope ratio between the isopycnal 1027.86 kg/m³ (approximately the
229 upper boundary of the dense overflow) and the bathymetry; **(b,e)** Depth-integrated PE to EKE conversion;
230 **(c,f)** Depth-integrated MKE to EKE conversion.

231 3.2 Genesis of subsurface eddies

232 As shown in Figs. 3(a) and 3(c), on the upper continental slope the negative vorticity may
233 become sufficiently nonlinear to form subsurface (below the pycnocline), coherent, cyclonic eddies.
234 These eddies have the same frequency as the TRWs, and originate from the trough mouth region
235 (blue dashed circle in Fig. 3(a)). A distinguishing feature of coherent eddies is their ability to transfer
236 material within their cores (Haller 2015), in contrast to the rectified Lagrangian transport that
237 occurs due to weakly nonlinear Rossby waves (e.g. Marshall et al. 2013). We illustrate the
238 coherence of the simulated eddies via a deployment of numerical Lagrangian floats at 300m depth

239 in our reference simulation, as shown in Fig. 5. This experiment shows that the stronger patches of
240 negative vorticity near the coast (located at $y \lesssim 35$ km) can "trap" the floats and convey them
241 westward within the eddy cores, indicating that these features are cyclonic coherent eddies. In
242 contrast, the broad patches of positive vorticity and the alternating structures further offshore do
243 not trap the floats, suggesting that these are quasi-linear TRWs.

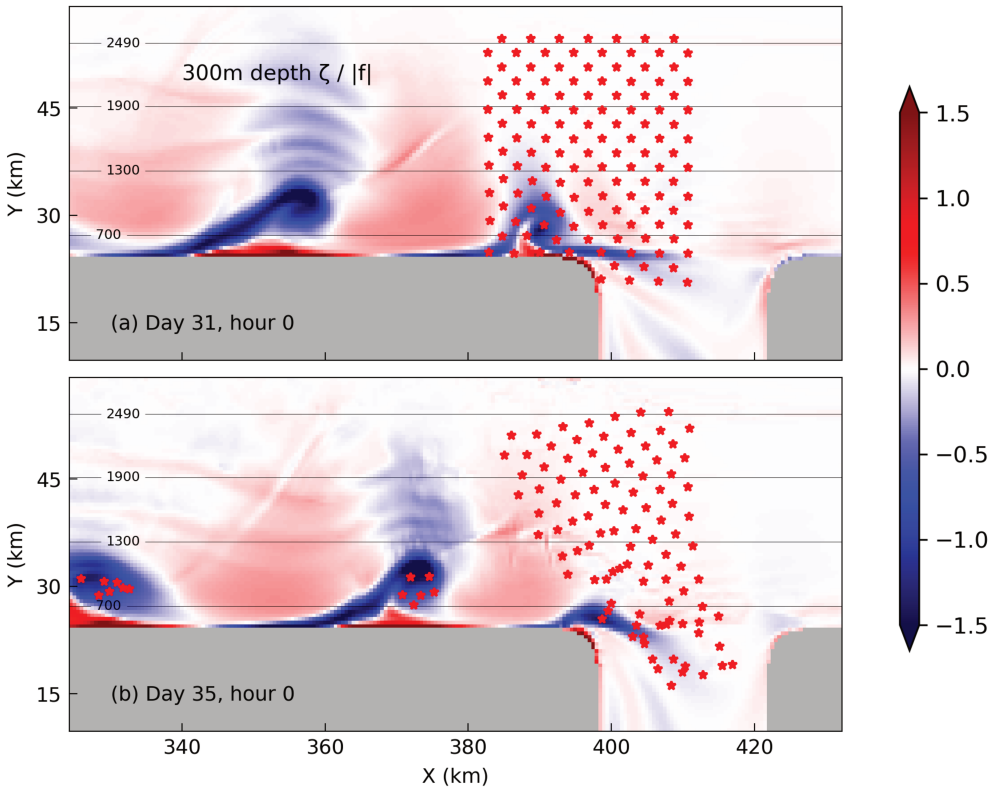


244

245 Figure 5. Float deployment experiment to identify nonlinear eddies. The color shading is the vertical relative
246 vorticity at 300m depth, normalized by the absolute Coriolis parameter. Contours indicate bathymetric depths
247 in meters. **(a)** The geopotential floats are released on day 31 at 300m depth; **(b)** The relative vorticity and
248 distribution of the floats after four days.

249 Genesis of eddies in oceanic overflows has previously been found in laboratory experiments
250 (Lane-Serff and Baines, 1998), in observations in the North Atlantic dense overflow (Spall and
251 Price, 1998; von Appen et al., 2014) and in numerical simulations (Wang et al., 2009; Nakayama
252 et al., 2014). Previous explanations for their formation have invoked vortex stretching (Lane-Serff

and Baines, 1998; Spall and Price, 1998). However, the period predicted by the vortex stretching theory is around 3 days in the Weddell Sea (Darelius et al., 2009), which is not consistent with the observed ~35h period. Here we propose that the genesis of the subsurface eddies is primarily a result of the nonlinear interaction between the TRWs and the overflow.

To identify the formation mechanism of the nonlinear eddies, we again utilize the EKE budget (Eqs. (2)-(6)). In Fig. 6 we plot spatial variations of the depth-integrated energy tendency terms specified in equation (2) in the vicinity of the trough mouth. The blue dashed circle in Fig. 6(a-d) approximately identifies the formation site of the subsurface eddies. In this region both the barotropic and baroclinic energy conversions are relatively weak (volume integrals yield $-1.6 \times 10^5\, J/s$ and $4.7 \times 10^5\, J/s$, respectively). In contrast, there is substantial energy convergence ($1.4 \times 10^6\, J/s$) here (Stewart and Thompson, 2016), which supplies the energy required to form the eddies. This suggests that the eastward transfer of energy by TRWs converges at the mouth of the trough, energizing perturbations in the dense outflow to the extent that they form nonlinear eddies. Note, however, that downstream of this formation site the eddies continue to grow, supported primarily by baroclinic energy production (Fig. 6(a-b)).

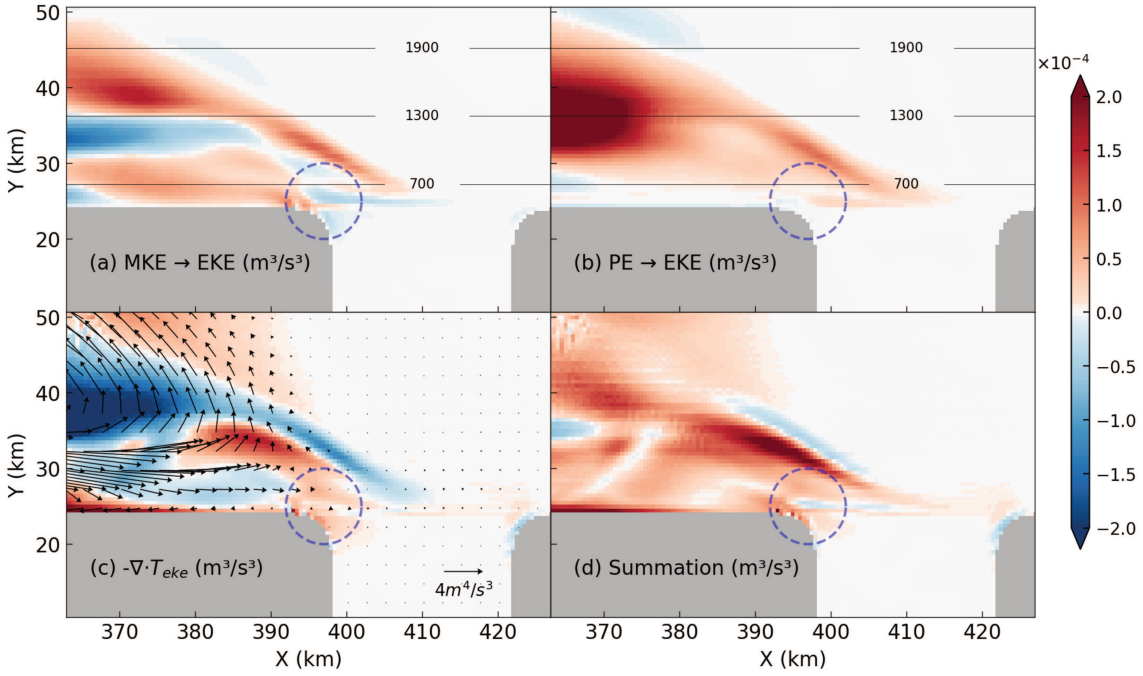

Figure 6. **(a-b)** Time-mean (over 6 TRW periods), depth-integrated energy conversions from MKE and PE to EKE, respectively; **(c)** The convergence of depth-integrated horizontal energy transport. The arrows indicate the direction of the depth-integrated energy transport ($\boldsymbol{T}_{\mathrm{eke}}$); **(d)** Total energy conversion ((a) + (b) + (c)). Contours indicate bathymetric depths in meters.

This mechanism is further supported by Fig. 7, which provides a process view of the formation of nonlinear eddies over a full TRW period: The outflow of DSW induces a background cyclonic motion in the overlying water at the trough mouth (Fig. 7a, Morrison et al., 2020). Due to the eastward propagation of energy, the TRW has a prominent signature even east of the trough mouth, and east of the regions in which EKE is produced (Fig. 6). The TRW has both cyclonic and anticyclonic phases that transit westward past the mouth of the trough. Fig. 7(b-e) show that as the cyclonic phase of the TRW approaches the western side of the trough mouth, it reinforces the background cyclonic motion and induces offshore motion that draws the fluid out onto the slope. The resulting vortex stretching (Lane-Serff and Baines, 1998) also leads to an intensification of the cyclonic relative vorticity in the overlying water leaving the trough mouth, and thus a nonlinear cyclonic eddy is formed. In contrast, as the anticyclonic phase of the TRW approaches the trough mouth, it is against the background cyclonic motion and induces onshore motion that suppresses the dense outflow, confining the fluid to the trough mouth and thus preventing eddy formation. This sequence of events explains not only the location and frequency of eddy generation, but also why there are only cyclonic eddies. In such a scenario, the formation of subsurface eddies depends crucially on the strength of the TRW feedback to the dense outflow. When the TRWs are suppressed, either by a background flow opposing the eastward wave energy propagation (Fig. 3(d-f)), or by a steeper slope (Fig. 3(g-i)), eddies are no longer generated.

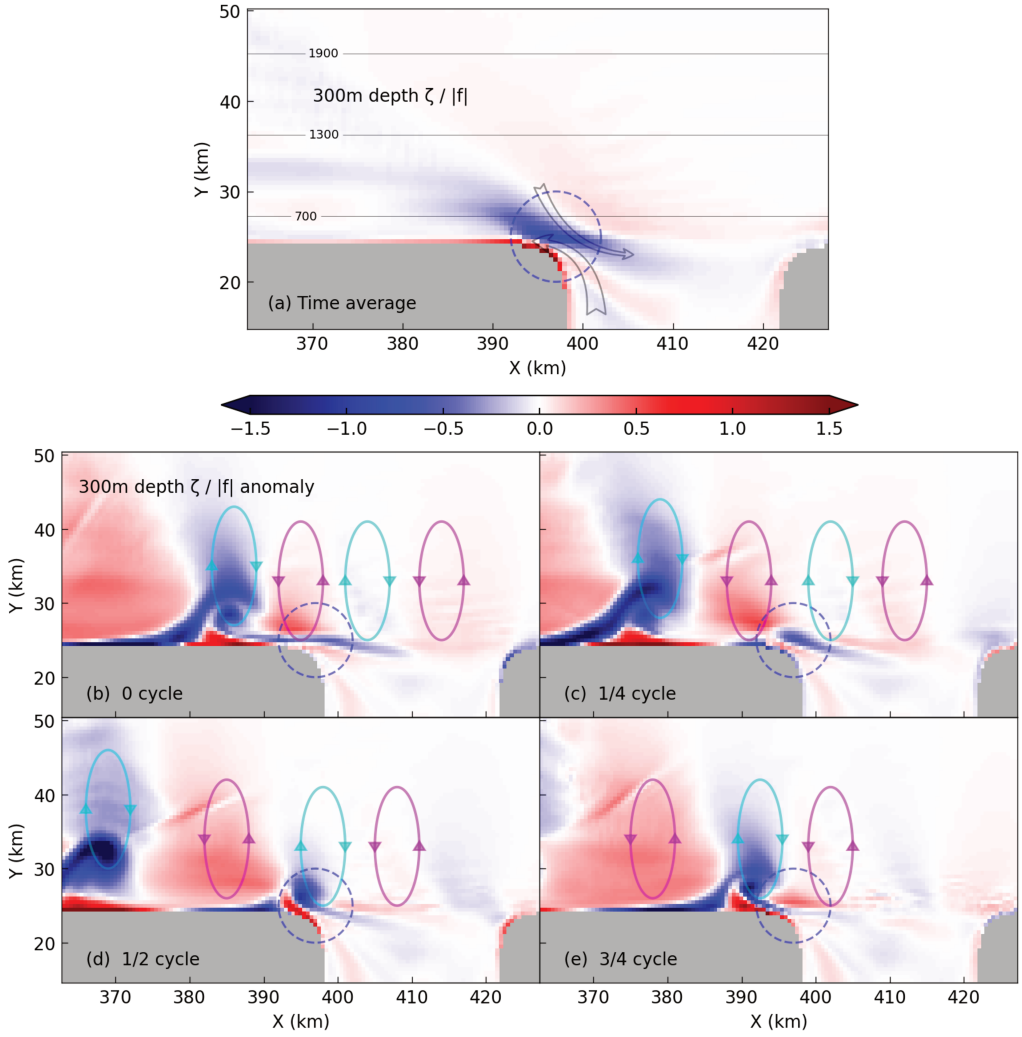


Figure 7. TRWs modulate subsurface eddy formation. (**a**) Time averaged relative vorticity at 300m depth. Grey arrows schematically indicate the direction of the time-mean flow at the trough mouth; **(b-e)** Snapshots of normalized vertical relative vorticity anomaly (relative to panel a) at 300m depth, separated by a time interval of 9 hours (approximately 1/4 cycle). The cyan and magenta ellipses schematically indicate clockwise and anti-clockwise TRWs circulations respectively. The blue dashed circles indicate the source region of the eddies.

### 3.3 Sensitivity to bathymetric slope and along-slope flow

In the preceding subsections we demonstrated that the dense water overflow exhibits three qualitatively different dynamical regimes: the overflow may be approximately steady, may support regular oscillations in the form of TRWs, or may generate coherent subsurface eddies at the trough mouth (see Fig. 3). We now investigate how the overflow transitions between these regimes as we

vary key control parameters, i.e. the topographic slope and the along-slope background flow. We interpret these transitions with the aid of linear TRW theory (Sec. 3.1) and the linear baroclinic instability theory of dense overflows (Swaters 1991).

Fig. 8(a) shows that the oscillation period is highly sensitive to the slope steepness, decreasing by a factor of 6 from ~115 h for $s = 0.02$ to ~20 h for $s > 0.12$. This dependence is closely predicted by the linear TRW theory. Fig. 8(b) shows that the oscillation period increases with increasing background flow (defined positive for eastward flow). Thus including a westward flow, in analogue with the Antarctic Slope Current, shortens the simulated TRW period, as seen earlier in Fig. 3(j). Fig. 8(c-d) display the dependences of EKE and the amplitude of the westward tracer flux fluctuations on slope steepness and background flow respectively. The tracer flux fluctuations and EKE approximately co-vary, indicating that the dense overflow is modulated by the coupled TRWs and subsurface eddies.

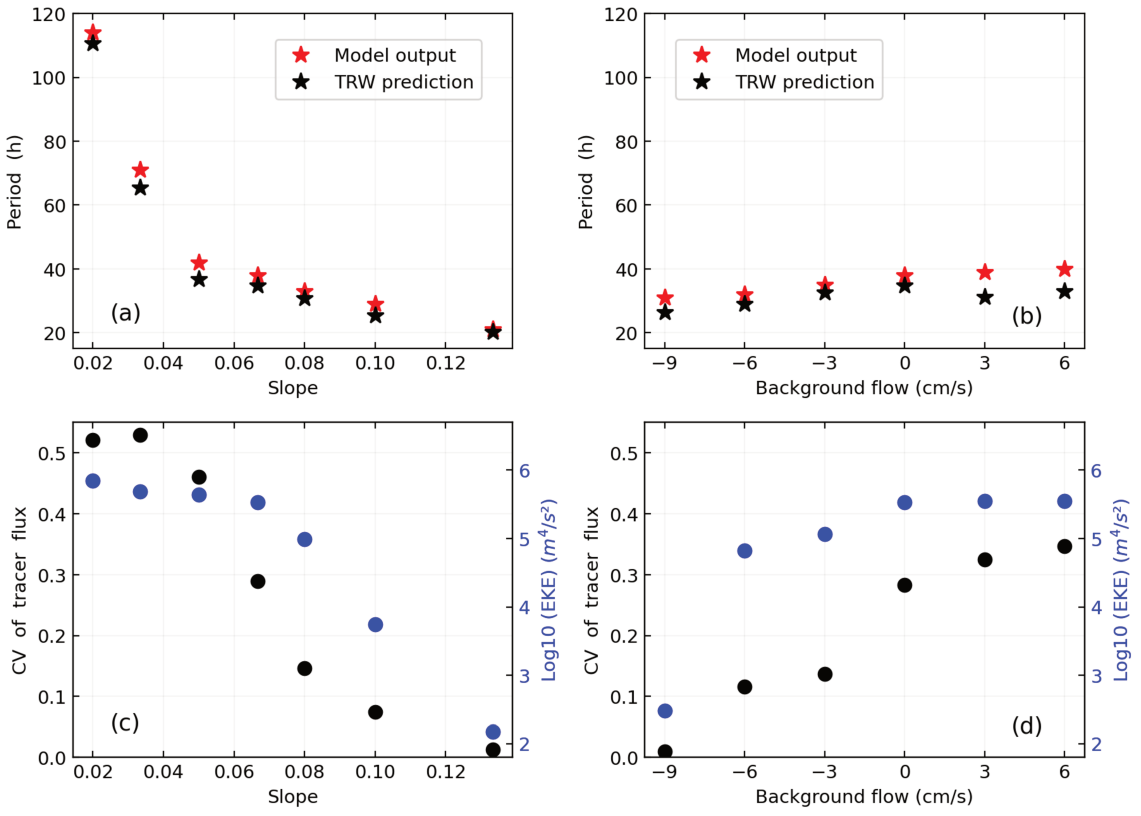

Figure 8. **(a)** Dependence of oscillation period on slope steepness (with zero background flow). Red stars indicate model diagnostics, and black stars indicate predictions of the linear TRW theory; **(b)** Dependence of oscillation period on background flow (with slope steepness $s = 1/15$); **(c)** Dependence of EKE and tracer flux fluctuations on slope steepness. The blue dots indicate depth-integrated EKE across the transect indicated by the green line in Fig. 3(a). The black dots indicate the coefficient of variation (CV, standard deviation / mean value) of the westward tracer flux at the same transect, quantifying the fluctuations of dense overflow transport; **(d)** Similar to panel (c) but for dependence on background flow, with a constant slope ($s = 1/15$).

Although the simulated TRWs closely adhere to the theoretical dispersion relationship (Fig. 8(a)), a caveat is that we obtain the wavelengths from model diagnostics rather than from an *a priori* theoretical prediction. According to the dispersion relationship (Equation (1)), it is the wavelength that determines the TRW frequency in specific experiment. Figs. 9(a) and 9(b) show the dependence of the diagnosed TRW wavelength ($\lambda_d$) on the slope steepness and the background flow speed, respectively. As the slope steepness decreases, the wavelength increases first and then remains around 40km for $s \lesssim 1/15$. In contrast, there is no significant trend for varying background flow if we omit the two cases (with eastward background flow) that have large uncertainties. The wavelength might also be expected to be related to the trough width, which introduces an independent lengthscale to the simulated flow. However, a sensitivity experiment shows nearly no changes when the trough width is doubled to 50km (not shown).

The TRW wavelength may be linked to the baroclinic instability of the dense overflow. Linear baroclinic instability theory (Swaters, 1991; Reszka et al., 2002) predicts that the most unstable wavelength is around tens of kilometers over a large parameter range, which is consistent with our model results. In addition, this theory predicts a high-wavenumber cutoff for baroclinic instability, which is expressed in the nondimensional form as

$$k_{max} = \sqrt{2\mu/a} + \sqrt{1 + 2\mu/a}\,. \qquad (7)$$

Here $\mu = \frac{h}{sR}$ is ``interaction parameter'' between the dense overflow and the overlying waters, $s$ is the slope steepness, $h$ is the overflow thickness, and $a$ is the overflow half-width

nondimensionalized by the Rossby deformation radius ($\mathrm{R} = NH/f$). We estimate the overflow width on the slope to be ~10 km (Fig. 3), and the deformation radius to be ~6 km in the overlying water. Since $k_{max}$ varies monotonically with $\mu$ (and thus $h$) and the thickness of dense overflow is arbitrary, depending on the isopycnal to define dense water, we take $h$ to be 100m and 300m respectively to estimate $k_{max}$. The corresponding dimensional minimum wavelength ($\lambda_{min}$) for baroclinic instability can be expressed as

$$\lambda_{min} = \frac{2\pi R}{k_{max}}. \qquad (8)$$

From Fig. 9, we can see that the diagnosed wavelength is larger than the predicted minimum wavelength cutoff for in almost all simulations, and thus the linear theory predicts that small-amplitude baroclinic waves should grow and generate TRWs in these simulations. For the steepest slopes examined here, the diagnosed TRW wavelength becomes comparable to or smaller than the minimum unstable wavelength, consistent with the suppression of TRWs in the $s = 2/15$ simulation. This results partly from the increase of $\lambda_{min}$with $s$, because steeper slopes result in a decrease in the interaction parameter $\mu$, and partly because the diagnosed wavelength decreases with $s$. Our results suggest that the latter results from the wavelength of the growing baroclinic modes being constrained by the width of the continental slope: Fig. 9(a) shows that for slopes greater than approximately $s = 1/15$, the diagnosed wavelength approximately tracks the continental slope width. This indicates that as the slope steepens, the range of unstable wavelengths steadily narrows due to the combined influences of the narrowing continental slope and the increasing wavelength cutoff for baroclinic instability.

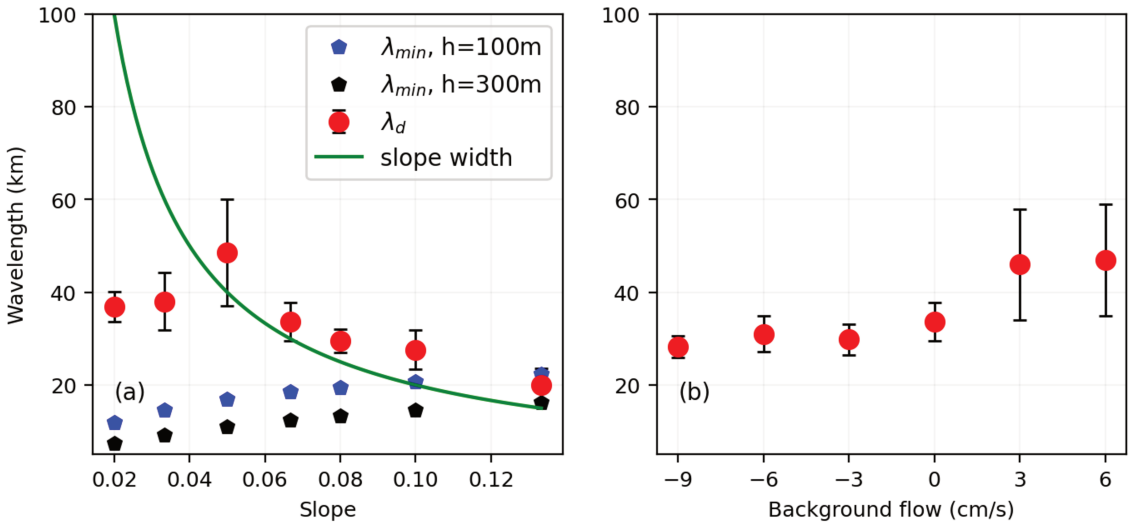


Figure 9. (**a**) Dependence of the TRW wavelength on slope steepness (with zero background flow). The red dots indicate the diagnosed TRW wavelength averaged over 6 wave periods. The blue and black pentagon markers indicate the minimum wavelength cutoff for linear baroclinic instability (Swaters, 1991) based on the dense overflow thicknesses of 100m and 300m, respectively. The green line shows the width of the continental slope. (**b**) Dependence of the TRW wavelength on background flow speed (with slope steepness $s = 1/15$). The error bars indicate the standard deviation.

We also note that the EKE varies dramatically for the cases with slope steepness $s > 1/15$, as does the variability of dense overflow (Fig. 8(c)). For the cases with no background flow, the only externally-imposed energy source is the dense inflow, including its kinetic energy and potential energy. As noted above, steep slopes suppress baroclinic instability and decrease the energy transition to overlying water, thus the EKE is relatively weak. We can also get similar conclusions through interaction parameter ($\mu$), since the interaction parameter decreases as the slope steepens, which indicates weaker interactions between dense overflow and overlying water. The theory of Swaters (1991) predicts that smaller $\mu$ leads to a smaller growth rate, consistent with the reduction in EKE for steeper slopes in Fig. 8(c). Furthermore, the unstable baroclinic modes may be further constrained to occur at shorter wavelengths as the continental slope narrows (Fig. 9a), which would further reduce the linear growth rate (Swaters 1991).

These results can explain the contrasting manifestations of TRWs in the Weddell Sea and Ross

Sea overflows. In the Weddell Sea, the continental slope is less steep, with a slope angle is approximately $s = 1/15$ close to the continental shelf break, which in our experiments permits a strong TRW signal. In contrast, the corresponding slope angle in the Ross Sea is $s{\sim}2/15$,which almost entirely suppress the production of TRWs in our model simulations. One exception is mooring EB in the Ross Sea overflow (Fig. 1(c)), which shows weak TRW signals with periods between 30-40h (Fig. 1(d)). This may be because the slope angle at this mooring is less steep ($s{\sim}1/15$), similar to the upper slope in the Weddell Sea.

The background flow primarily influences the EKE and the tracer fluctuations by suppressing (for westward flows) or enhancing (for eastward flows) the eastward energy transport by TRWs (Fig. 8(d)). For strong westward background flow, TRWs will develop further downstream. Since we diagnose the EKE and tracer fluctuations at a fixed downstream section shown in Fig. 3f, these variables change dramatically with varying westward flows.

## 4. Conclusion

Dense overflow oscillations are routinely observed on the continental slope of the southern Weddell Sea and in other oceanic overflows (Darelius et al., 2009, 2015; Spall and Price, 1998; Oshima et al., 2013), but not in the Ross Sea overflow (Ou et al., 2009). In this study, we investigate the dynamical controls of these oscillations with the aid of a process-oriented simulations (Fig. 2), and identify steady, wavy and eddying regimes across a range of along-slope flow and slope steepnesses (Fig. 3 and Fig. 8).

Dense overflows over continental slopes are intrinsically unstable (Swaters, 1991) and thus energize coupled TRWs that oscillate throughout the water column (Section 3.1). If the group velocity (energy) of the TRWs is eastward, the propagation of waves may exert a feedback on the outflow at the trough mouth (Fig. 6). Mechanistically, this feedback occurs because the alternating vorticity anomalies of the TRW reinforce or suppress the outflow and the associated background

cyclonic motion, resulting in cyclonic subsurface eddies that have the same frequency as the TRW (Section 3.2, Fig. 7). These eddies can modulate the dense overflow through pressure forces, producing convergence and divergence via bottom Ekman transport (Lane-Serff and Baines, 1998), and thus increasing the oscillations in the flux of dense water. Eventually the dense overflow is structured as a series of periodic cold eddies, as has been observed in the Weddell Sea (Daae et al., 2019).

In our experiments, we investigate the parameter dependence by changing the slope steepness and the background along-slope flow. A steep slope can almost entirely suppress the production of TRWs and eddies, and instead results in a steady, along-slope, geostrophic dense overflow, as observed in the Ross Sea (Fig. 1(c-d)). In Sec. 3.3 we post that this occurs because the steeper slopes result in an increase in the minimum wavelength that is baroclinically unstable (Swaters 1991), combined with a suppression of longer-wavelength instabilities as the continental slope narrows. Varying the slope steepness also leads to dramatic changes in the EKE and the behavior of the dense overflow. For less steep continental slopes ($s \lesssim 1/15$), the wavelength of the TRWs is relatively insensitive to changes in the model parameters (Fig. 9). In this regime the oscillation period increases relatively rapidly as the slope steepness decreases, in qualitative agreement with the linear baroclinic instability theory (Swaters, 1991). This may explain the longer oscillation periods in the Denmark Strait overflow (2-3 days) (Spall and Price, 1998) and the Faroe Bank Channel overflow (3-6 days) (Darelius et al., 2015), where the slopes are less steep.

Including a background along-slope flow also has significant impact on the oscillation period and the EKE downstream of the dense water outflow. A strong enough westward background flow can suppress the eastward TRW energy propagation, and thus the formation of subsurface eddies. However, our simulations suggest that the westward background flows do not necessarily need to be stronger than the group velocity of TRWs to suppress the eastward energy propagation, e.g. a background flow with the speed of -6 cm/s can suppress the upstream energy propagation efficiently and prevent the formation of eddies (Fig. 3(d)), even though the diagnosed group

433 velocity is 13 cm/s in our reference case. A plausible explanation for this is that the overall eastward
434 propagation speed of the TRW energy (including advection of the mean flow) must be sufficiently
435 large in order for the energy to reach the trough mouth before it is dissipated by bottom friction.

436 Previous studies have suggested that formation of coherent eddies may occur directly as a
437 result of baroclinic instability (Swaters, 1991) or vortex stretching (Lane-Serff and Baines, 1998).
438 However, the linear baroclinic instability theory predicts the formation of cyclonic eddies on the
439 downslope side of the plume (Swaters 1991; Jungclaus et al., 2001), which is not consistent with
440 observations and our model results. Although it is difficult to reconcile with the linear theory, the
441 energy in the eddies is largely or entirely sourced from baroclinic energy release (Fig. 4(c-d)),
442 depending on whether a background flow is imposed. We can also discard vortex stretching
443 mechanism as a trigger for coherent eddy formation, because there is no eddy formation without
444 the modulation of TRWs (Fig. 3(d-i)), even if the outflow-induced background cyclonic motions
445 still occur at the trough mouth. However, we cannot exclude vortex stretching as a contributing
446 factor in the formation of subsurface eddies, because the TRW-induced eddy formation may be
447 accompanied by water column stretching, and because stretching favors cyclonic vorticity
448 generation. Therefore, while baroclinic instability and vortex stretching should not be neglected,
449 our results indicate that TRWs play a fundamental role in the genesis of coherent eddies in the
450 dense water outflow.

451 Finally, we note that our simulations are rather idealized to simplify the dynamical analysis.
452 We do not include tidal forcing, which is typically strong in the Weddell Sea and the Ross Sea, and
453 potentially influences the hydrography and dynamics there (Semper and Darelius, 2017; Padman
454 et al., 2009; Daae et al., 2019). The coastal wall in our model setup, which is not present in real
455 Antarctic overflows, may also influence the properties of TRWs. However, based on the theory of
456 Swaters (1991), the onshore boundary does not change the properties of TRWs significantly as long
457 as the distance between the overflow and the onshore boundary is finite. In addition, the results in
458 this study are qualitatively consistent with other previous studies with no coastal wall, e.g. the

period of TRWs increase as the slope steepness decrease, and the wavelengths of the TRWs are consistently around 50km (Marques et al., 2014). This suggests that the presence of the coastal wall does not substantially influence the results of our experiments. Another idealization is the initialization of the simulations with stratification based on summer measurements that exhibit a strong pycnocline. In nature the pycnocline is eroded in winter time, which will shift the dispersion curve (Semper and Darelius, 2017) and change the properties of TRWs generated by dense overflow. We also use linear slopes, which may limit the range of TRW modes that occur over the continental slope. In contrast, *in situ* observations have revealed three primary oscillation frequencies in the southern Weddell Sea, concentrated on the upper, middle and lower slopes respectively, each of which have different slope steepnesses (Darelius et al., 2009).

In summary, this study characterizes the different dynamical regimes that may occur in dense water overflows on continental slopes, quantifies the transitions between these regimes as the topographic slope and background flow vary, and offers insights into the mechanisms of coherent eddy generation and TRW suppression. However, explicit predictive theories for the amplitudes of the eddies and TRWs are still lacking, and the roles of these processes in producing the rectified downslope transport of dense water are still in need of further investigation. As a final note, we point out that although the subsurface eddies manifest unambiguously in our simulations, detecting their structure in the field is challenging and warrants attention in future observational campaigns.

**Acknowledgments:** The authors thank Arnold L. Gordon for sharing the mooring data in the Ross Sea. This study was supported by the Natural Science Foundation of China (41730535), the National Key R&D Program of China (2019YFC1509102), and the Impact and Response of Antarctic Seas to Climate Change Program (01-01-01B, 02-01-02). A.L.S. acknowledges support from the National Science Foundation under Grant Number OCE-1751386.

## Open Research

The matlab scripts for the generation of numerical simulations and the configurations of ROMS are available at: https://doi.org/10.5281/zenodo.6778078. The moorings data used in this study are available under

https://doi.org/10.1594/PANGAEA.792882

https://doi.org/10.1594/PANGAEA.792883

https://doi.org/10.1594/PANGAEA.792884

https://doi.org/10.1594/PANGAEA.792885

https://doi.org/10.1594/PANGAEA.869787

https://doi.org/10.1594/PANGAEA.869788

https://doi.org/10.1594/PANGAEA.869789

https://doi.org/10.1594/PANGAEA.869790

https://doi.org/10.1594/PANGAEA.869791

https://doi.org/10.1594/PANGAEA.870447

https://doi.org/10.1594/PANGAEA.870448

https://doi.org/10.1594/PANGAEA.870446

https://doi.org/10.1594/PANGAEA.870449

# References


Von Appen, W. J., Pickart, R. S., Brink, K. H., & Haine, T. W. N. (2014). Water column structure and statistics of denmark strait overflow water cyclones. Deep-Sea Research Part I: Oceanographic Research Papers, 84, 110–126. https://doi.org/10.1016/j.dsr.2013.10.007

Daae, K., Fer, I., & Darelius, E. (2019). Variability and mixing of the Filchner overflow plume on the continental slope, Weddell sea. Journal of Physical Oceanography, 49(1), 3–20. https://doi.org/10.1175/JPO-D-18-0093.1

Darelius, E., Smedsrud, L. H., Østerhus, S., Foldvik, A., & Gammelsrød, T. (2009). Structure and variability of the Filchner overflow plume. Tellus, Series A: Dynamic Meteorology and Oceanography, 61(3), 446–464. https://doi.org/10.1111/j.1600-0870.2009.00391.x

Darelius, E., Fer, I., Rasmussen, T., Guo, C., & Larsen, K. M. H. (2015). On the modulation of the periodicity of the Faroe Bank Channel overflow instabilities. Ocean Science, 11(5), 855–871. https://doi.org/10.5194/os-11-855-2015

Fahrbach, E., Woodgate, R. A., Rohardt, G. (2012a): Physical oceanography and current meter data from mooring F1. Alfred Wegener Institute, Helmholtz Centre for Polar and Marine Research, Bremerhaven, PANGAEA, https://doi.org/10.1594/PANGAEA.792882

Fahrbach, E., Woodgate, R. A., Rohardt, G. (2012b): Physical oceanography and current meter data from mooring F2. Alfred Wegener Institute, Helmholtz Centre for Polar and Marine Research, Bremerhaven, PANGAEA, https://doi.org/10.1594/PANGAEA.792883

Fahrbach, E., Woodgate, R. A., Rohardt, G. (2012c): Physical oceanography and current meter data from mooring F3. Alfred Wegener Institute, Helmholtz Centre for Polar and Marine Research, Bremerhaven, PANGAEA, https://doi.org/10.1594/PANGAEA.792884

Fahrbach, E., Woodgate, R. A., Rohardt, G. (2012d): Physical oceanography and current meter data from mooring F4. Alfred Wegener Institute, Helmholtz Centre for Polar and Marine Research, Bremerhaven, PANGAEA, https://doi.org/10.1594/PANGAEA.792885

Fer, I. (2016a): Current measurements in the southern Weddell Sea at mooring site M1. Geophysical Institute, University of Bergen, PANGAEA, https://doi.org/10.1594/PANGAEA.869787

Fer, I. (2016b): Current measurements in the southern Weddell Sea at mooring site M2. Geophysical Institute, University of Bergen, PANGAEA, https://doi.org/10.1594/PANGAEA.869788

Fer, I. (2016c): Current measurements in the southern Weddell Sea at mooring site M3. Geophysical Institute, University of Bergen, PANGAEA, https://doi.org/10.1594/PANGAEA.869789

Fer, I. (2016d): Current measurements in the southern Weddell Sea at mooring site M4. Geophysical Institute, University of Bergen, PANGAEA, https://doi.org/10.1594/PANGAEA.869790

Fer, I. (2016e): Current measurements in the southern Weddell Sea at mooring site M5. Geophysical Institute, University of Bergen, PANGAEA, https://doi.org/10.1594/PANGAEA.869791

Foldvik, A., Gammelsrød, T., Øterhus, S., Fahrbach, E., Rohardt, G., Schröder, M., et al. (2004). Ice shelf water overflow and bottom water formation in the southern Weddell Sea. Journal of Geophysical Research: Oceans, 109(2), 1–15. https://doi.org/10.1029/2003jc002008

Foldvik, A., Gammelsrød, T., Østerhus, S. (2017a): Temperature and current measurements in the Weddell Sea at mooring site S2-1987. Geophysical Institute, University of Bergen, PANGAEA, https://doi.org/10.1594/PANGAEA.870446

Foldvik, A. (2017b): Temperature and current measurements in the Weddell Sea at mooring site S3. Geophysical Institute, University of Bergen, PANGAEA, https://doi.org/10.1594/PANGAEA.870449

Gordon, A. L., Orsi, A. H., Muench, R., Huber, B. A., Zambianchi, E., & Visbeck, M. (2009). Western Ross Sea continental slope gravity currents. Deep-Sea Research Part II: Topical Studies in Oceanography, 56(13–14), 796–817. https://doi.org/10.1016/j.dsr2.2008.10.037

Gula, J., Molemaker, M. J., & McWilliams, J. C. (2016). Topographic generation of submesoscale centrifugal instability and energy dissipation. *Nature communications*, *7*(1), 1-7.

Guo, C., Ilicak, M., Fer, I., Darelius, E., & Bentsen, M. (2014). Baroclinic instability of the Faroe Bank Channel overflow. Journal of Physical Oceanography, 44(10), 2698–2717. https://doi.org/10.1175/JPO-D-14-0080.1

Haller, G. (2015). Lagrangian coherent structures. Annu. Rev. Fluid Mech, 47(1), 137-162.

Ilicak, M., Adcroft, A. J., Griffies, S. M., & Hallberg, R. W. (2012). Spurious dianeutral mixing and the role of momentum closure. Ocean Modelling, 45–46, 37–58. https://doi.org/10.1016/j.ocemod.2011.10.003

Isachsen, P. E. (2015). Baroclinic instability and the mesoscale eddy field around the Lofoten Basin. *Journal of Geophysical Research: Oceans*, *120*(4), 2884-2903. https://doi.org/10.1002/2014JC010448

Jensen, M. F., Fer, I., & Darelius, E. (2013). Low frequency variability on the continental slope of the southern Weddell Sea. Journal of Geophysical Research: Oceans, 118(9), 4256–4272. https://doi.org/10.1002/jgrc.20309

Johnson, G. C. (2008). Quantifying Antarctic Bottom Water and North Atlantic Deep Water volumes. Journal of Geophysical Research: Oceans, 113(5), 1–13. https://doi.org/10.1029/2007JC004477

Jungclaus, J. H., Hauser, J., & Käse, R. H. (2001). Cyclogenesis in the Denmark Strait overflow plume. *Journal of Physical Oceanography*, *31*(11), 3214-3229. https://doi.org/10.1175/1520-0485(2001)031<3214:CITDSO>2.0.CO;2

Lane-Serff, G. F., & Baines, P. G. (1998). Eddy formation by dense flows on slopes in a rotating fluid. Journal of Fluid Mechanics, 363, 229–252. https://doi.org/10.1017/S0022112098001013

Legg, S., Hallberg, R. W., & Girton, J. B. (2006). Comparison of entrainment in overflows simulated by z-coordinate, isopycnal and non-hydrostatic models. Ocean Modelling, 11(1–2), 69–97. https://doi.org/10.1016/j.ocemod.2004.11.006

Legg, S., Briegleb, B., Chang, Y., Chassignet, E. P., Danabasoglu, G., Ezer, T., et al. (2009). Improving Oceanic Overflow Representation in Climate Models. Bulletin of the American Meteorological Society, 90(5), 657–670. https://doi.org/10.1175/2008BAMS2667.I

Marques, G. M., Padman, L., Springer, S. R., Howard, S. L., & Özgökmen, T. M. (2014). Topographic vorticity waves forced by Antarctic dense shelf water outflows. Geophysical Research Letters, 41(4), 1247–1254. https://doi.org/10.1002/2013GL059153

Marshall, D. P., Vogel, B., & Zhai, X. (2013). Rossby rip currents. Geophysical research letters, 40(16), 4333-4337.

Morrison, A. K., McC. Hogg, A., England, M. H., & Spence, P. (2020). Warm Circumpolar Deep Water transport toward Antarctica driven by local dense water export in canyons. Science Advances, 6(18), 1–10. https://doi.org/10.1126/sciadv.aav2516

Nakayama, Y., Ohshima, K. I., Matsumura, Y., Fukamachi, Y., & Hasumi, H. (2014). A numerical investigation of formation and variability of Antarctic bottom water off Cape Darnley, East Antarctica. Journal of Physical Oceanography, 44(11), 2921–2937. https://doi.org/10.1175/JPO-D-14-0069.1

Nof, D. (1983). The translation of isolated cold eddies on a sloping bottom. *Deep Sea Research Part A, Oceanographic Research Papers*, *30*(2), 171–182. https://doi.org/10.1016/0198-0149(83)90067-5

Ohshima, K. I., Fukamachi, Y., Williams, G. D., Nihashi, S., Roquet, F., Kitade, Y., et al. (2013). Antarctic Bottom Water production by intense sea-ice formation in the Cape Darnley polynya. Nature Geoscience, 6(3), 235–240. https://doi.org/10.1038/ngeo1738

Ou, H. W., Guan, X., & Chen, D. (2009). Tidal effect on the dense water discharge, Part 1: Analytical model. Deep-Sea Research Part II: Topical Studies in Oceanography, 56(13–14), 874–883. https://doi.org/10.1016/j.dsr2.2008.10.031

Padman, L., Howard, S. L., Orsi, A. H., & Muench, R. D. (2009). Tides of the northwestern Ross Sea and their impact on dense outflows of Antarctic Bottom Water. Deep-Sea Research Part II: Topical Studies in Oceanography, 56(13–14), 818–834. https://doi.org/10.1016/j.dsr2.2008.10.026

Reszka, M. K., Swaters, G. E., & Sutherland, B. R. (2002). Instability of abyssal currents in a continuously stratified ocean with bottom topography. Journal of Physical Oceanography, 32(12), 3528–3550. https://doi.org/10.1175/1520-0485(2002)032<3528:IOACIA>2.0.CO;2

Semper, S., & Darelius, E. (2017). Seasonal resonance of diurnal coastal trapped waves in the southern Weddell Sea, Antarctica. Ocean Science, 13(1), 77–93. https://doi.org/10.5194/os-13-77-2017

Shchepetkin, A. F., & McWilliams, J. C. (2003). A method for computing horizontal pressure-gradient force in an oceanic model with a nonaligned vertical coordinate. Journal of Geophysical Research: Oceans, 108(3), 1–34. https://doi.org/10.1029/2001jc001047

Spall, M. A., & Price, J. F. (1998). Mesoscale variability in Denmark strait: The PV outflow hypothesis. Journal of Physical Oceanography, 28(8), 1598–1623. https://doi.org/10.1175/1520-0485(1998)028<1598:MVIDST>2.0.CO;2

Stewart, A. L., & Thompson, A. F. (2015). Eddy-mediated transport of warm Circumpolar Deep Water across the Antarctic shelf break. *Geophysical Research Letters*, *42*(2), 432-440. https://doi.org/10.1002/2014GL062281

Stewart, A. L., & Thompson, A. F. (2016). Eddy generation and jet formation via dense water outflows across the Antarctic continental slope. Journal of Physical Oceanography, 46(12), 3729–3750. https://doi.org/10.1175/JPO-D-16-0145.1

Swaters, G. E. (1991). On the baroclinic instability of cold-core coupled density fronts on a sloping continental shelf. Journal of Fluid Mechanics, 224, 361–382. https://doi.org/10.1017/S0022112091001799

Pedlosky, J. (1987). Geophysical fluid dynamics (Vol. 710). New York: springer.

Talley, L. D. (2013). Closure of the global overturning circulation through the Indian, Pacific, and southern oceans. Oceanography, 26(1), 80–97. https://doi.org/10.5670/oceanog.2013.07

Wang, Q., Danilov, S., & Schröter, J. (2009). Bottom water formation in the southern Weddell Sea and the influence of submarine ridges: Idealized numerical simulations. Ocean Modelling, 28(1–3), 50–59. https://doi.org/10.1016/j.ocemod.2008.08.003

Woodgate, R. A., Fahrbach, E., Schröder, M., Rohardt, G., Nicholls, K. W. (2017a): Temperature and current measurements in the Weddell Sea at mooring site Fr1. Alfred Wegener Institute for Polar and Marine Research, Bremerhaven (1986-2013), PANGAEA, https://doi.org/10.1594/PANGAEA.870447

Woodgate, R. A., Fahrbach, E., Schröder, M., Rohardt, G., Nicholls, K. W. (2017b): Temperature and current measurements in the Weddell Sea at mooring site Fr2. Alfred Wegener Institute for Polar and Marine Research, Bremerhaven (1986-2013), PANGAEA, https://doi.org/10.1594/PANGAEA.870448

Zhao, B., & Timmermans, M. L. (2018). Topographic Rossby Waves in the Arctic Ocean's Beaufort Gyre. *Journal of Geophysical Research: Oceans*, *123*(9), 6521–6530. https://doi.org/10.1029/2018JC014233